



## Article

# Effect of Ferromagnetic Metal Base on Friction and Wear of 3D-Printed Aluminum Alloy Surface under Magnetorheological Fluid Action

Deyong Li <sup>1</sup>, Rui Li <sup>2</sup> and Chul-Hee Lee <sup>1,\*</sup>

<sup>1</sup> Department of Mechanical Engineering, Inha University, Incheon 22212, Republic of Korea; lideyong@inha.edu

<sup>2</sup> School of Automation, Chongqing University of Posts and Telecommunications, Chongqing 400065, China; lirui@cqupt.edu.cn

\* Correspondence: chulhee@inha.ac.kr; Tel.: +82-32-860-7311

**Abstract:** This study aimed to enhance the friction performance and controllable range of magnetorheological devices by investigating the impact of different materials on the tribological properties within a magnetorheological fluid (MRF) under the influence of a magnetic field. A novel friction-combined structure was proposed, consisting of a ferromagnetic metal base and a metal surface shell fabricated using 3D printing technology. The design offered several advantages: the ferromagnetic base significantly improved the magnetic field control range, the 3D-printed surface shell allowed easy replacement with different materials and textures, and it reduced both development and application costs. In this experimental study, composite samples consisting of metal 3D-printed surfaces and substrates made of different materials were used to evaluate the friction and wear characteristics of the MRF under different magnetic field conditions. Computer numerical control (CNC)-machined surfaces were also included for comparison. The results showed that the ferromagnetic matrix affected the magnetic field size and distribution of the energized coil, resulting in an increase in the friction coefficient, but also an increase in wear. Furthermore, the combination of 3D-printed surfaces with ferromagnetic substrates had a more pronounced effect on the friction coefficient compared to CNC-machined surfaces. Based on these findings, this research concluded that 3D-printed surfaces outperform CNC-machined surfaces in this specific environment. In addition, the proposed design, which combined ferromagnetic bases with 3D-printed surfaces, shows potential for improving the friction performance of friction components. The increase rate of friction coefficient from 0.1459 at no current to 0.2089 at 2.5A was 43.18%. This offers a novel application of 3D printing technology in magnetorheological devices.

**Keywords:** ferromagnetic metal; magnetorheological fluid; 3D printing; surface shell; wear



**Citation:** Li, D.; Li, R.; Lee, C.-H. Effect of Ferromagnetic Metal Base on Friction and Wear of 3D-Printed Aluminum Alloy Surface under Magnetorheological Fluid Action. *Lubricants* **2023**, *11*, 273. <https://doi.org/10.3390/lubricants11070273>

Received: 23 May 2023

Revised: 17 June 2023

Accepted: 21 June 2023

Published: 23 June 2023



**Copyright:** © 2023 by the authors. Licensee MDPI, Basel, Switzerland. This article is an open access article distributed under the terms and conditions of the Creative Commons Attribution (CC BY) license (<https://creativecommons.org/licenses/by/4.0/>).

## 1. Introduction

Ferromagnetic materials are magnetized into magnetic conductors by the action of an external magnetic field [1]. The magnetic conductors are magnetic and if they have enough magnetism, they will change the distribution of magnetic field strength under a magnetic field [2]. Magnetorheological fluids (MRFs) are intelligent materials with controllable rheological behavior [3] and are widely used in many fields [4]. For example, magnetorheological fluids are used to control stability [5] and lubricity [6]. The suspended particles in the MRF are ferromagnetic materials. In the magnetic field, these ferromagnetic particles are arranged along the lines of magnetic force under the influence of the magnetic force, thereby affecting the viscosity and shear force of the magnetorheological fluid, causing the magnetorheological effect [7].

The magnetorheological effect means that the magnetorheological fluid exhibits different viscosities and fluidity under different magnetic field strengths [8], and even solid-like

properties if the magnetic field is strong enough [9]. MRFs to be widely used in various applications such as dampers [10], clutch systems [11], and sealing systems [12]. The wear parts in the existing research on friction and wear of magnetorheological fluids are all integrated structures, which are typically CNC-machined [13,14].

Metal 3D printing employs a unique rapid cooling process that results in the production of fine grains. This approach offers significant advantages over traditional manufacturing methods, enabling the establishment of a comprehensive control mechanism for integrated additive manufacturing that encompasses material, process, microstructure, and performance [15]. However, the inherent defects, residual stresses, and microstructural properties associated with additive manufacturing can have a significant impact on structural components, particularly those sensitive to fracture and fatigue properties [16]. Performance characteristics such as fatigue crack growth rate, fracture toughness, and fatigue strength must be considered along with techniques to improve the damage tolerance of alloys [17,18].

During the 3D printing process, the rapid solidification of the melt induces a microstructure like that achieved with rapid quenching techniques. This microstructure is characterized by fine, metastable constituent phases with enhanced solid solubility. The printed layers are repeatedly heated and cooled, resulting in complex thermal cycles that predominantly lead to the formation of columnar grains and the presence of residual stresses [19]. These unique microstructural features, spanning multiple length scales from nanometers to millimeters, distinguish the mechanical properties of 3D-printed metal materials from those of conventionally manufactured counterparts [20].

In contrast to the low cooling rate and formation of secondary dendrites in conventional casting processes, the selective laser melting (SLM) process has an extremely high cooling rate ( $>10^6$  K/s) [21], which prevents the formation of secondary dendrites and results in a cellular morphology [22]. As a result, the mechanical properties of the aluminum alloy (AlSi10Mg) printed by the SLM process show significant improvements compared to those processed conventionally [23,24]. However, the layer-by-layer deposition of metal powder and subsequent laser sintering in the SLM process can lead to spheroidization and the presence of tiny holes in the printed product. Surprisingly, these defects can be advantageous in certain studies. Spheroidization and tiny holes reduce the frictional contact area between the component surface and the test ball during friction tests, like the metal hand-scraping technique [25] that incorporates dimples to reduce the coefficient of friction [26].

This study represents the first application of metal 3D printing to wear parts exposed to magnetorheological fluid. However, since 3D-printed materials are not inherently ferromagnetic, a set of experiments with different material substrates and processing surfaces was designed to perform friction and wear tests. After bonding the 3D-printed metal surface sheet to the metal substrate of the two materials, the friction and wear of the surface sheet was evaluated in the presence of magnetorheological fluid using constant current excitation of the coil. A control group consisting of a CNC-machined aluminum alloy surface was evaluated under identical conditions. By comparing the data from the two sets, the influence of the 3D printing processing method on the experiment was determined. In addition, the effect of the ferromagnetic metal substrate on the magnitude and distribution of the magnetic field intensity generated by the coil was simulated using ANSYS. The relationship between magnetic field, friction, and wear was investigated to demonstrate the feasibility of the combined design. Ultimately, it was concluded that under the same electromagnetic coil current conditions, the combined sample of ferromagnetic metal substrate and 3D-printed surface exhibited a significant improvement in friction performance while effectively resisting deformation of the worn part.

## 2. Preparation

### 2.1. Magnetorheological Fluid

The MRF required for the experiment had to have the following characteristics: large dynamic yield strength difference, which ensures that the MRF can influence the friction effect under different magnetic field conditions; temperature resistance, which prevents the heat generated by friction and wear from affecting the experimental results; easy redispersion, the ability to flow back quickly after a pin passes through it; and non-corrosive [27,28]. MRF-132DG has properties such as fast response time, dynamic yield strength, temperature resistance, stiff settling resistance, non-abrasive [29], etc. Thus, MRF-132DG can meet the requirements of this research. The specific information is shown in Table 1.

**Table 1.** Data for MRF-132DG.

Item	Unit	Content
Viscosity	Pa·s	$0.112 \pm 0.02$
Density	$\text{g}/\text{cm}^3$	2.95–3.15
Solids Content by Weight	%	80.98
Flash Point	$^{\circ}\text{C}$	>150
Operating Temperature	$^{\circ}\text{C}$	−40~130

### 2.2. Sample Preparation

Selective laser melting (SLM), a metal 3D printing technique, was used to fabricate cylindrical noodles of aluminum alloy material (AlSi10Mg) with a diameter of 30 mm and a thickness of 2 mm. To evaluate the effect of metal 3D printing on metal friction, an experiment was conducted using CNC-machined surface plates as a control group under identical conditions. In the experiment, a cylindrical substrate with a diameter of 30mm and a thickness of 10mm was created using both steel (ferromagnetic metal) and aluminum alloy (non-ferromagnetic metal). The surface plate and substrate were then fused into a single unit. Figure 1 shows the resulting samples: (a) a sample with an aluminum alloy surface and an aluminum alloy substrate, and (b) a sample with an aluminum alloy surface and a steel base, (c) and (d) the combination of inspection patterns for the CNC-machined surface. The metal performance of 3D-printed parts of aluminum alloy was better than that of traditional casting parts, as shown in Table 2.

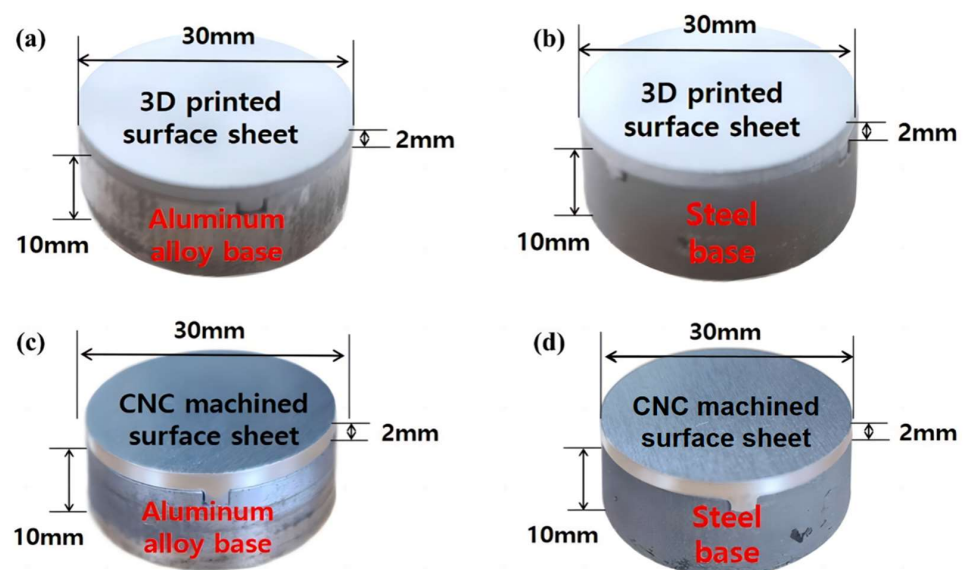


**Figure 1.** Samples in different combinations. (a) 3D-printed surface + aluminum alloy base; (b) 3D-printed surface + Steel base; (c) CNC-machined surface + aluminum alloy base; (d) CNC-machined surface + Steel base.

**Table 2.** Comparison of metal properties of 3D-printed parts of aluminum alloy and traditional casting parts.

Item	3D-Printed	Traditional Casting
Tensile Strength (Mpa)	400~460	220~300
Yield Strength (Mpa)	240~300	140~200
Elongation (%)	2~4	1~3
Hardness (HBW)	120~160	70~100

### 3. Experiment

#### 3.1. Friction and Wear Test

The friction and wear test of the sample combination using magnetorheological fluid (MRF) as a lubricant in the electromagnetic coil is shown in Figure 2a. To mitigate the effect of metal parts within the wear test system on the energized coil, Figure 2b shows the schematic of the actual component assembly. In this setup, all metal parts within the coil were replaced with high strength Poly-lactic acid (PLA) 3D-printed parts. The hardness and young's modulus of the PLA material were sufficient to withstand the 100N load applied during the friction and wear test without deformation or breakage.

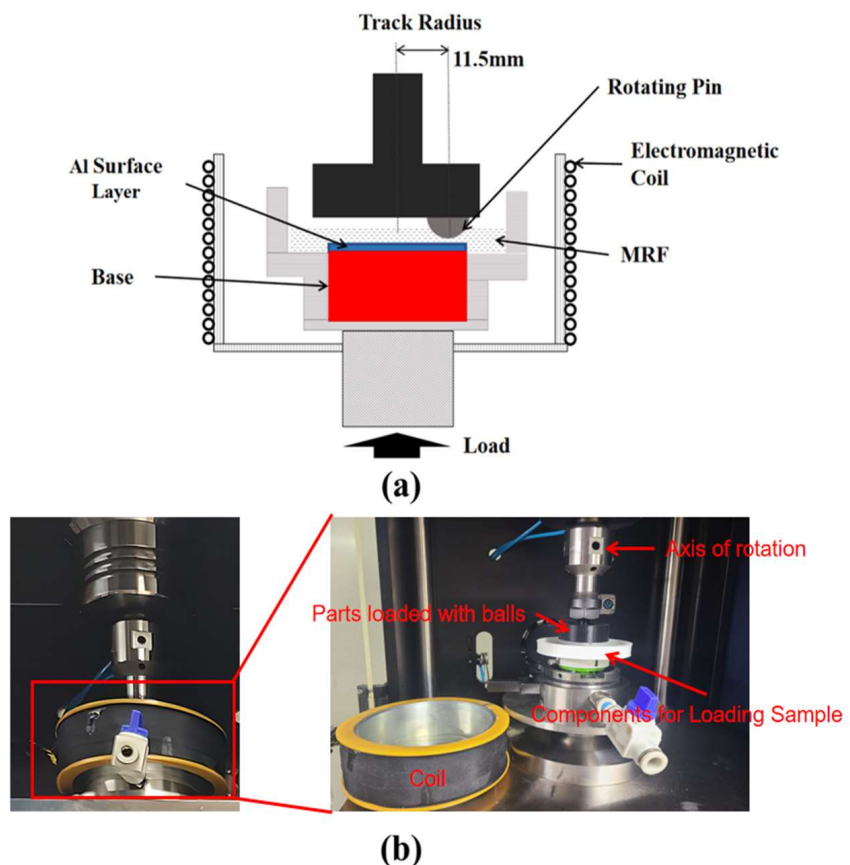


**Figure 2.** (a) Design drawing of wear test parts; (b) physical objects of wear test part.

The samples were subjected to a friction and wear test with MRF as a lubricant using a wear test system. As shown in Table 3, the abrasion test was carried out for 3600 s at a frequency of 50 rpm and a load of 100 N on a contact point with a radius of 11.5 mm, and the data on the change in coefficient of friction with time during the abrasion test were continuously recorded. In addition, the coated specimens shall be ultrasonically cleaned for 30 min before and after the abrasion test to prevent the presence of surface deposits from affecting the test results. Three tests were performed for each group combination and

the coefficient of friction was averaged. The result with the smallest error was then used to plot a line graph.

**Table 3.** Test conditions of wear test.

Parameter	Unit	Content
Speed	rpm	50
Test Radius	mm	11.5
Lubricant	-	MRF
Temperature	°C	15–25
Load	N	100
Duration	Sec	3600

### 3.2. Surface Analysis

The scar profile of each combined sample was magnified 200 times, overall and detailed scar photographs were taken, and the 3D image of the scar was constructed using image superposition technology. The 3D micrographs can more clearly show the grooves and plastic deformation of the wear marks. The width of the wear scars were evaluated using the measuring function in the microscope software.

Use a surface roughness tester to evaluate the wear mark profile at the location shown in Figure 3. The measuring range of the surface roughness tester was set to 4 mm. For a more accurate measurement, the part of the line segment on the friction surface that rotates around the axis of the cylindrical specimen and intersects the wear mark was selected for measurement. The included angle of the adjacent line segments was 90° and the measurement results were averaged. A line graph of the scar profile was output based on the data from the measurement points. In addition, the maximum depth of the scar and the height of the deformed part were output after calibrating the zero value.

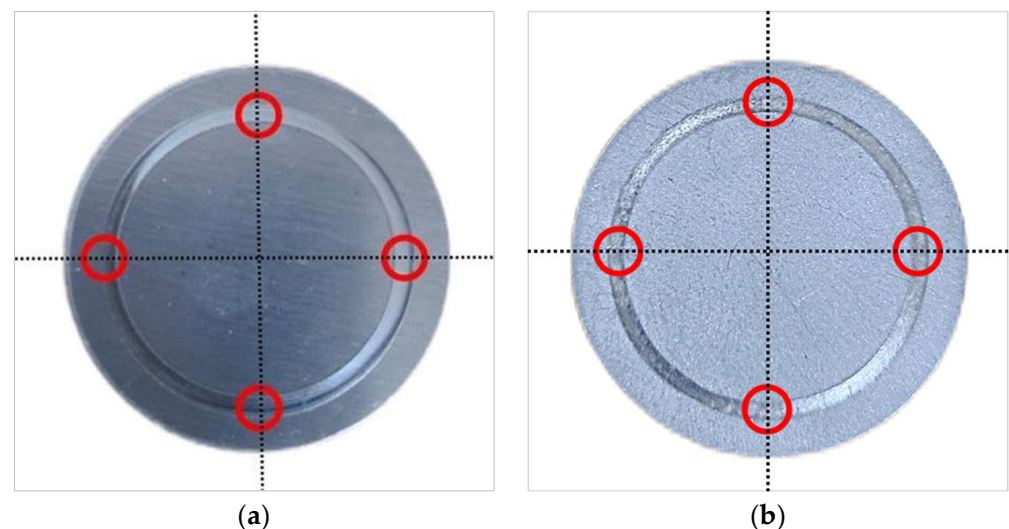


**Figure 3.** The surface roughness test location of the sample, the dotted line in the figure represents the axis of symmetry, and the red circle represents the position of the surface roughness test. (a) CNC-machined surface, (b) 3D-printed surface.

The average of the evaluation surface analysis results was taken. The result with the smallest error was then used to generate a line graph.

#### 4. Magnetostatic Simulation

We used the magnetostatic module of ANSYS 2022 R1 to construct the model of the same size combined specimen in the electromagnetic coil. We analyzed the magnetic field strength on the surface of the aluminum alloy when the material data of mild steel and aluminum alloy were added to the base of the combined specimen. The magnetic field strength of the aluminum alloy, surface-aluminium alloy base, and the aluminum alloy surface-steel base in the electromagnetic coil simulated by ANSYS is shown in Figure 4.

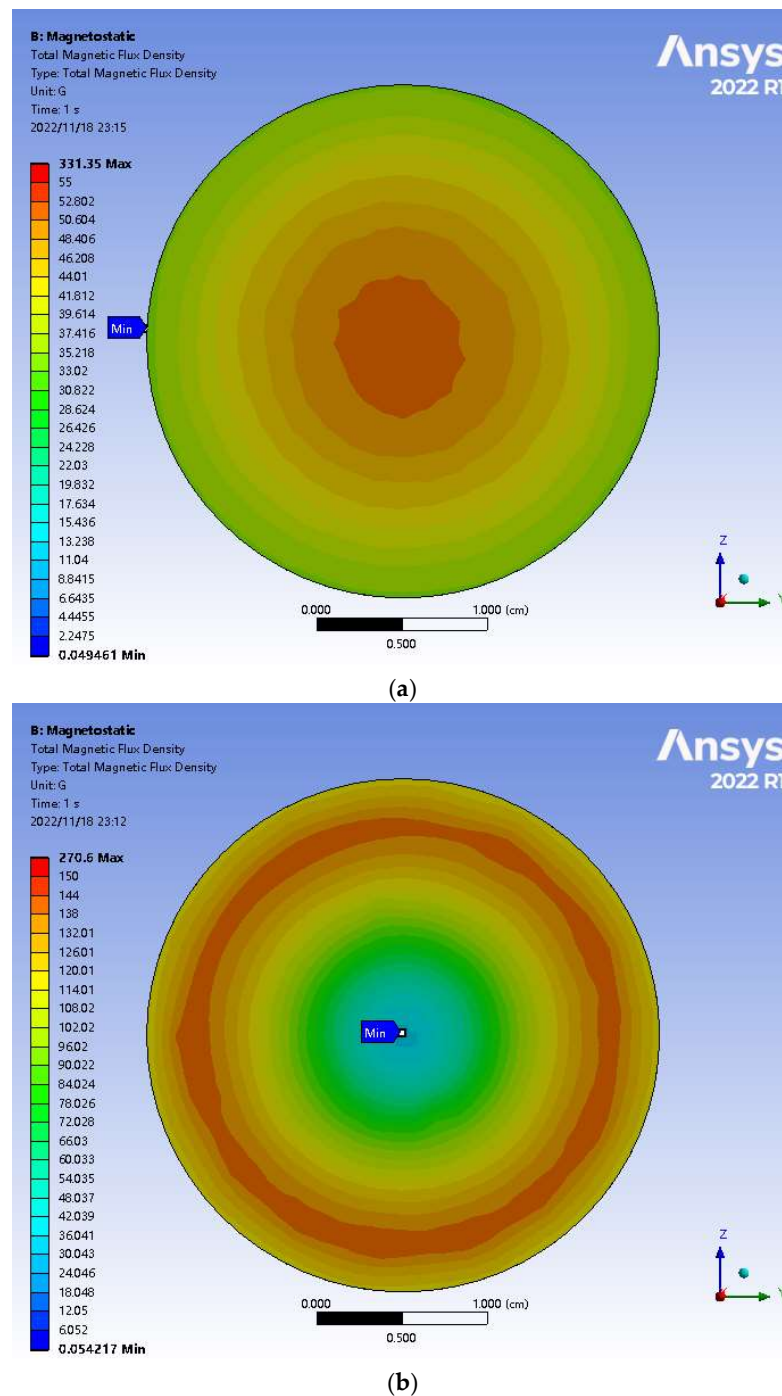
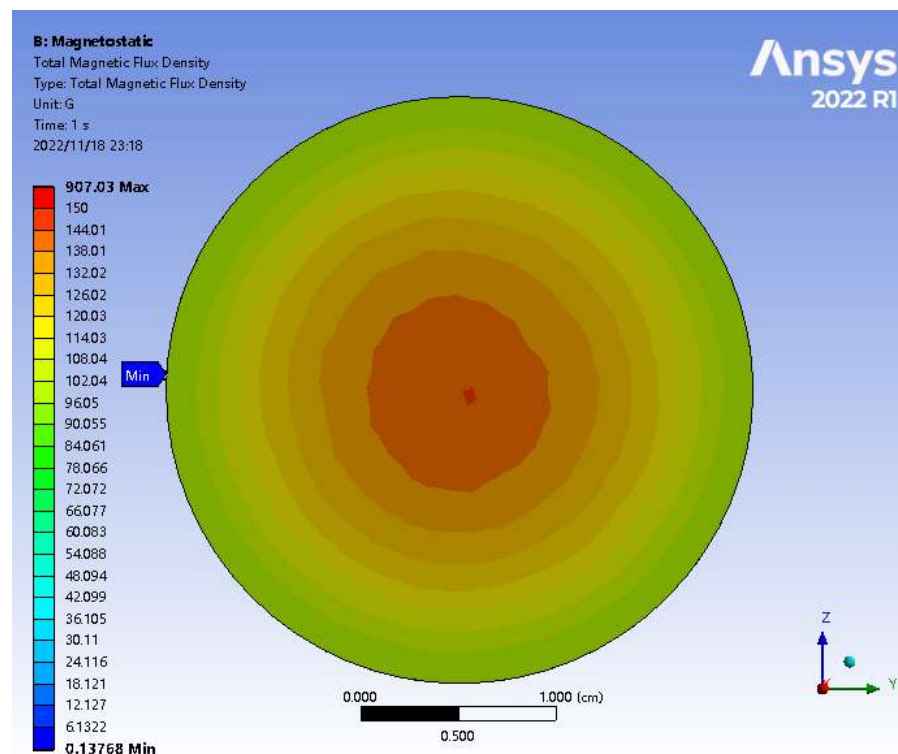


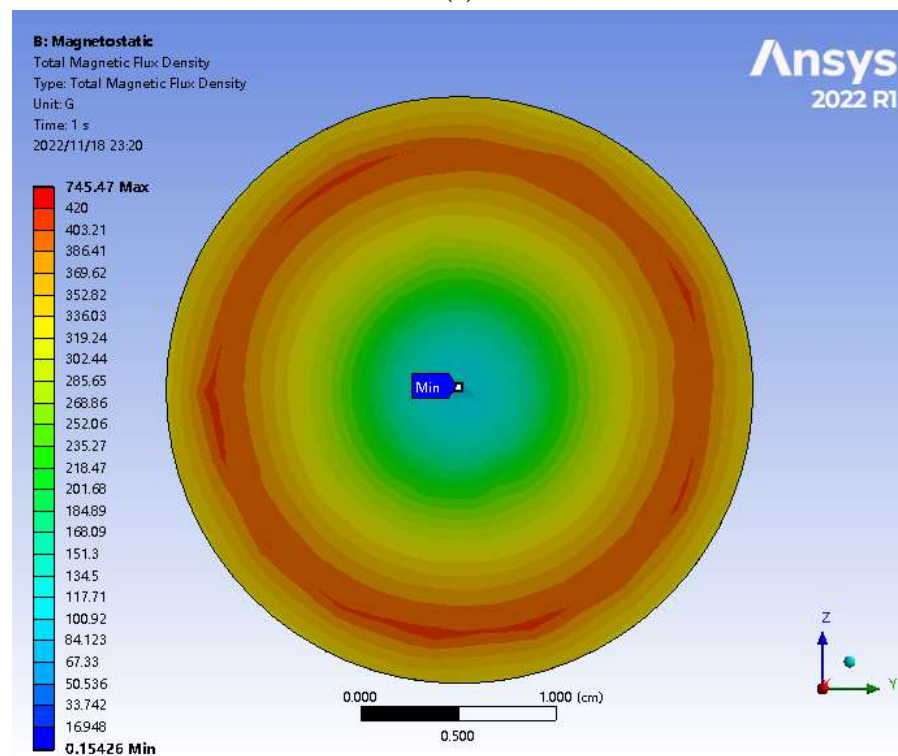
**Figure 4.** When the current of the energized coil = 0.8A, ANSYS simulation results of magnetic field strength on aluminum alloy surface. The blue markers represent the locations with the lowest magnetic fields. (a) aluminum alloy base (Access Date: 23:15, 18 November 2022), (b) steel base (Access Date: 23:12, 18 November 2022).

Comparing the evaluation of the surface magnetic field strength of different combined specimens simulated by ANSYS, the magnetic field intensity on the surface of the steel base combined specimen was more significant than that on the surface of the aluminum alloy-base combined specimen under the same current condition. When the base of the combined sample was aluminum alloy, the magnetic field intensity was concentrated towards the center of the wafer. When the base of the combined sample was steel, the magnetic field intensity distribution concentrated toward the edge of the surface [30]. The reason for this change in magnetic field distribution is that the sample was inside the electromagnetic coil. The electromagnetic coil can be regarded as a magnet when it is energized, so it was equivalent to the sample being in the inner center of the magnet as shown in Figure 4a. The magnetic field strength followed the direction of the magnetic induction line, which pointed towards the center of the magnet. When a ferromagnetic metal was placed in an electromagnetic coil, it was magnetized and became a magnet. At this point, the surface layer was on the surface of the ferromagnetic metal base, which was equivalent to being outside the magnetic pole of the magnet. The direction of the magnetic field line was bent and pointed to the other side. The magnetic field line of a magnetic pole at the center was inclined to the edge to form the magnetic field distribution shown in Figure 4b. Since the distance moved at the edge was the largest during the rotation, the utilization rate of the frictional force was the largest; the distance moved at the center of the circle was the smallest, and the utilization rate of the frictional force was low. Therefore, this magnetic field distribution of the steel base sample had a higher utilization rate of the magnetic field.

Figure 5 shows the magnetic flux distribution across the surface of various base combinations when the current was set to 2.5A. An observation showed that the magnetic flux distribution on the combined surface of the two bases was very similar to that shown in Figure 4, where the current was set to 0.8A. A notable difference, however, was that the magnetic flux was amplified approximately three times and was directly proportional to the current. Notably, at 2.5A, the maximum magnetic flux observed on the iron base combination surface was the same as that observed on the aluminum alloy base combination surface, indicating comparable magnetic effects.



(a)



(b)

**Figure 5.** When the current of the energized coil = 2.5A, ANSYS simulation results of magnetic field strength on aluminum alloy surface. The blue markers represent the locations with the lowest magnetic fields. (a) aluminum alloy base (Access Date: 23:18, 18 November 2022), (b) steel base (Access Date: 23:20, 18 November 2022).



## 5. Results and Discussion

Figure 6 shows the friction test results of four composite specimens for two types of surfaces and two types of bases when the electromagnetic coil currents were 0 A, 0.8 A and 2.5 A, respectively. Observing the friction test results shown in Figure 5, it can be concluded that the friction coefficient of the composite sample with steel base was greater than that of the composite sample with aluminum alloy base under the same current conditions (excluding current = 0). This effect of 3D-printed surfaces in metal was stronger than CNC-machined surfaces.

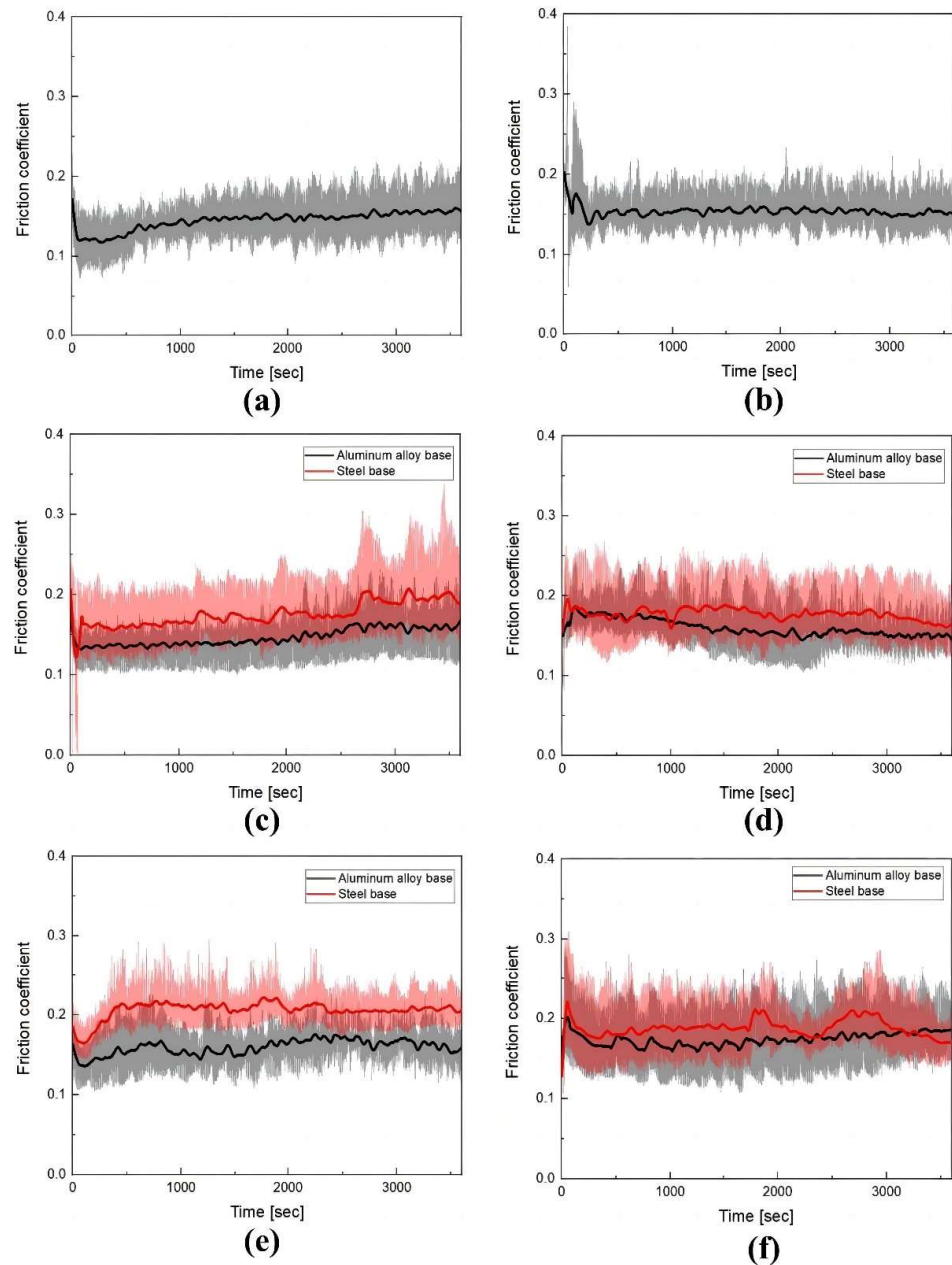


**Figure 6.** Friction coefficient of 3D-printed surface and CNC-machined surface under different conditions. The material of the base will not be affected when there is no electromagnetic field, so no legend is added to the line diagram when the current = 0, and the shaded part of the line diagram represents the fluctuation of the friction coefficient. (a) Current = 0 A, 3D-printed surface; (b) Current = 0 A, CNC-machined surface; (c) Current = 0.8 A, 3D-printed surface; (d) Current = 0.8 A, CNC-machined surface; (e) Current = 2.5 A, 3D-printed surface; (f) Current = 2.5 A, CNC-machined surface.

Figure 7 displays histogram of friction coefficient data for two different surface materials across various experimental groups. The range within the chart indicates the fluctuation range of the friction coefficient, the bars represent the average value of the friction coefficient, the two standard deviation horizontal lines above and below the average value indicate the concentration range of the friction coefficient, and outliers means that the value that only appeared once or twice in the whole experiment process was a pure error and cannot be included in the calculation.

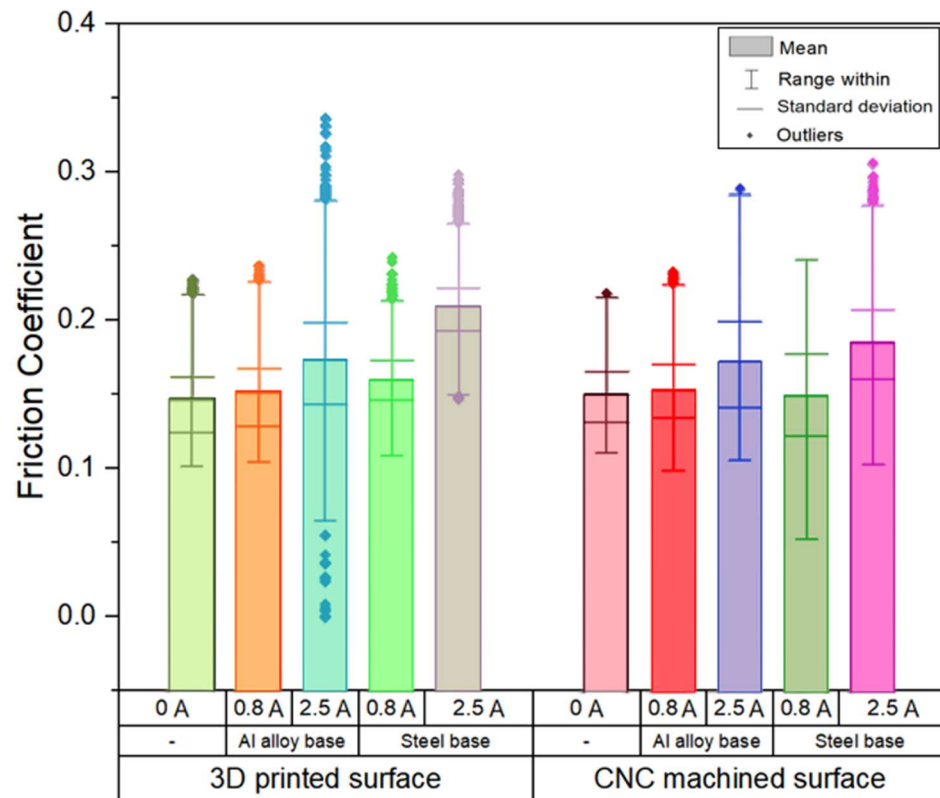
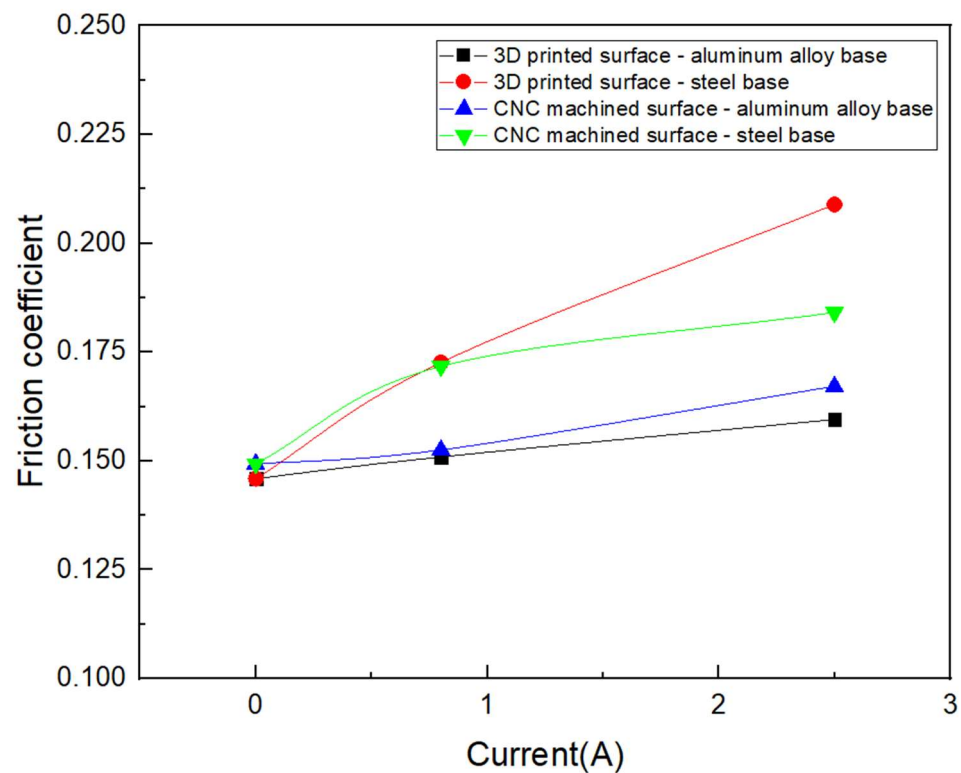


Figure 7. Histogram of coefficient of friction for different experimental groups.

Upon observation, increasing the voltage resulted in significantly higher friction performance on the 3D-printed surface as compared to the CNC-machined surface. Furthermore, the steel base group exhibited stronger and more stable friction performance on the same 3D-printed surface when compared to the aluminum base group.

The specific influence of the steel base on the coefficient of friction can be seen in Figure 8 and Table 4. Observing the dotted line of the change in the coefficient of friction of different combinations in Figure 8, the metal 3D-printed steel base sample combination had the most obvious change in the coefficient of friction with increasing current. When the coil current was increased to 2.5 A, the friction coefficient of the metal 3D-printed surface-steel matrix composite sample increased by 43.18%, while the friction coefficient of the CNC-machined surface-steel matrix composite sample increased by 23.31%. The magnetizability of the base under the energized coil current had a greater effect on the coefficient of friction of the metal 3D-printed surfaces than that of the CNC-machined surfaces. This could be due to the complex texture of the 3D-printed metal surface, which contained voids. The magnetorheological effect of MRF had a more pronounced effect on the coefficient of friction of surfaces with more complex textures.

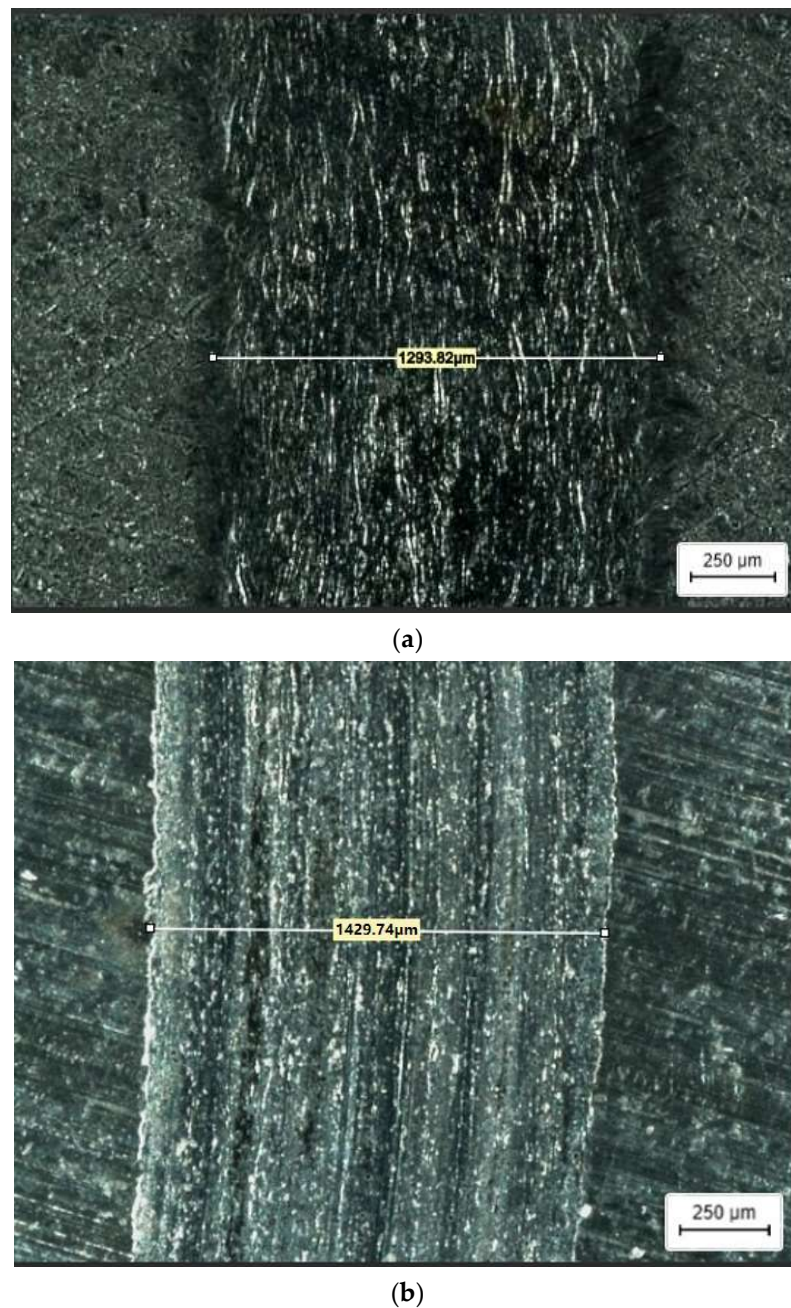


**Figure 8.** The line chart of the change of friction coefficient of different combination samples with the change of current.

**Table 4.** Summary of friction test evaluation results.

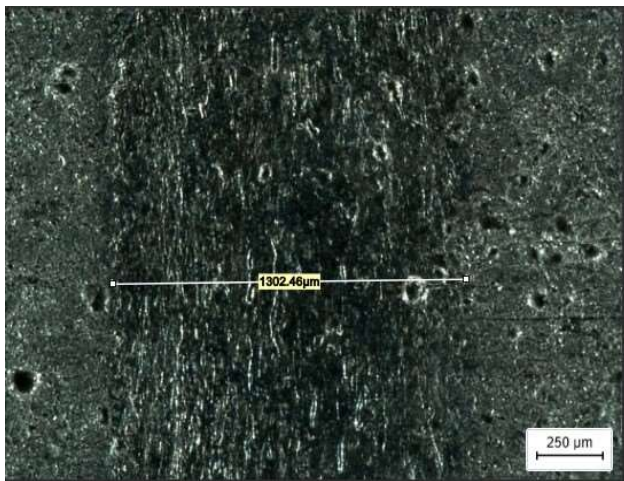
Surface	Base	Current (A)	Friction Coefficient		Growth Rate (%)
			Avg.	Sta. Dev	
Metal 3D printing	-	0	0.1459	0.0011	-
Metal 3D printing	Aluminum alloy	0.8	0.1509	0.0016	3.43
Metal 3D printing	Steel	0.8	0.1726	0.0018	18.30
Metal 3D printing	Aluminum alloy	2.5	0.1595	0.0012	9.32
Metal 3D printing	Steel	2.5	0.2089	0.0013	43.18
CNC machining	-	0	0.1493	0.0009	-
CNC machining	Aluminum alloy	0.8	0.1525	0.0012	2.14
CNC machining	Steel	0.8	0.1717	0.0019	15.00
CNC machining	Aluminum alloy	2.5	0.1671	0.0018	11.92
CNC machining	Steel	2.5	0.1841	0.0016	23.31

Figure 3 shows the worn section of the sample, and it was important to select the micrograph and worn section with the score closest to the average for a meaningful comparison. Figure 9 shows photomicrographs showing wear marks on both the 3D-printed metal surface and the CNC-machined surface without stress. When comparing these surfaces, it was apparent that the wear marks on the 3D-printed metal surface appeared rougher but narrower than the CNC-machined surface. However, closer inspection revealed that the rough grooves on the worn part of the metal 3D-printed surface were not a result of additional wear, but rather a characteristic of the 3D printing process. These distinctive dimples played a role in reducing the frictional contact area between the component surface and the test ball during friction testing, like the application of dimples in the metal hand-scraping technique to reduce the coefficient of friction. This explains why the metal 3D-printed surface had a lower coefficient of friction than the CNC-machined surface in the absence of current.

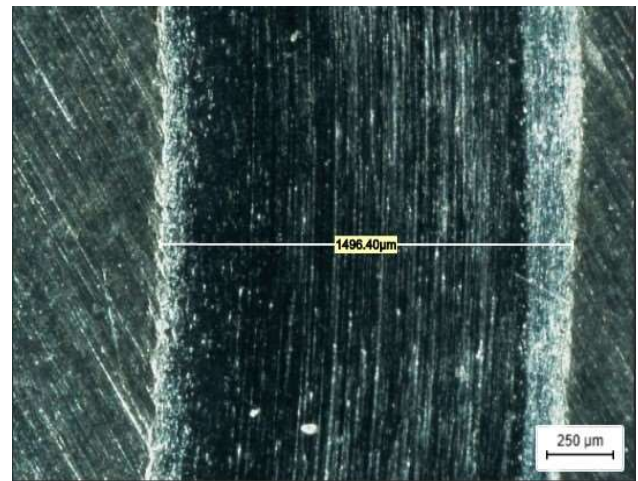


**Figure 9.** Surface wear marks of each control group sample under current = 0 A. (a) 3D-printed surface; (b) CNC-machined surface.

Figure 10 shows compelling micrographs that meticulously capture the wear marks etched on the surfaces of both the 3D-printed metal and CNC-machined samples in this scenario. When comparing the two, the wear marks on the 3D-printed metal surface exhibited a rougher texture characterized by distinct and pronounced ridges. These rough ridges were primarily due to the inherent voids created during the 3D printing process itself. However, a fascinating phenomenon occurred when the magnetorheological fluid (MRF) within these grooves underwent magnetization effects. The strong shear force exerted by the MRF within these grooves served to accelerate the increase in the test value of the coefficient of friction.



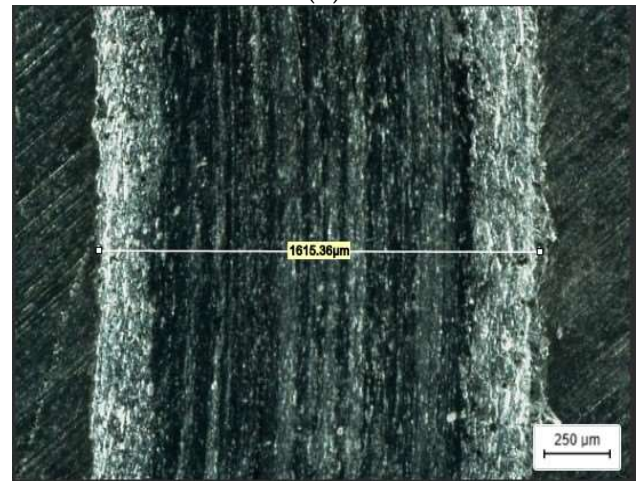
(a)



(b)



(c)



(d)



(e)



(f)

Figure 10. Cont.

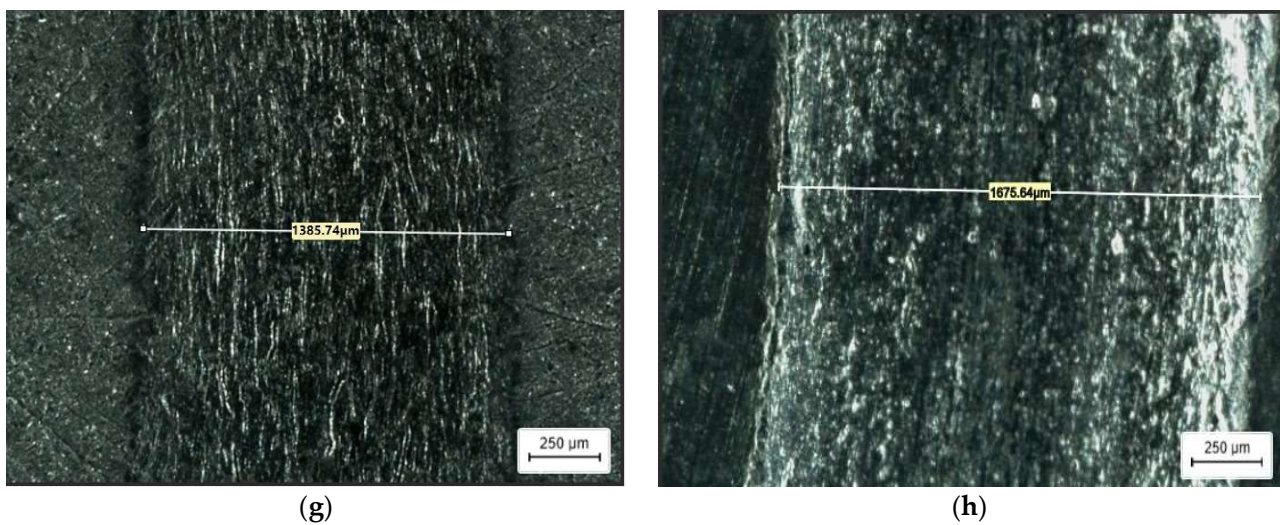


**Figure 10.** Surface wear marks of each control group sample under the optical microscope. (a) Current = 0A, 3D-printed surface; (b) Current = 0A, CNC-machined surface; (a) Current = 0.8A, 3D-printed surface—Al base; (b) Current = 0.8A, CNC-machined surface—Al base; (c) Current = 0.8A, 3D-printed surface—steel base; (d) Current = 0.8A, CNC-machined surface—steel base; (e) Current = 2.5A, 3D-printed surface—Al base; (f) Current = 2.5A, CNC-machined surface—Al base; (g) Current = 2.5A, 3D-printed surface—steel base; (h) Current = 2.5A, CNC-machined surface—steel base.

There was also an interesting relationship between the width of the wear marks and the applied stress. On the metal 3D-printed surface, the width of the wear marks showed a decreasing trend as the stress increased. Conversely, the width of the wear marks on the CNC-machined surface showed an increasing trend with increasing stress. In addition, when the wear marks of the aluminum alloy base combination were considered, their width decreased with increasing current. Conversely, the width of the wear traces for the combined samples showed an increasing trend with increasing current.

These compelling findings shed light on the intricate interplay between voltage/current variations and the resulting wear trace widths for different surface combinations. The observations provide valuable insights into the effects of 3D printing, magnetorheological fluid behavior, and voltage/current manipulation on the frictional properties of the materials studied.

Figure 11 is a contour line drawing of the wear traces of the metal 3D-printed surface and the CNC-machined surface under different conditions. The wear scar profile of the metal 3D-printed surface was rougher, but the wear scar profile on the CNC-machined surface was deeper and more deformed due to the presence of small pores on the 3D-printed metal surface that form a honeycomb structure, increasing resistance to deformation.

The wear test results of each experimental group are presented in Table 5, and the results are depicted as histograms in Figure 12. When tested under identical conditions, the CNC-machined surface exhibited significantly greater wear width and depth than the 3D-printed surface. However, the test results for the 3D-printed surface had a wider fluctuation range than the CNC-machined surface, and the range increased with voltage. In addition, at the same voltage, the steel base group showed larger test results and fluctuations than the aluminum alloy base group.

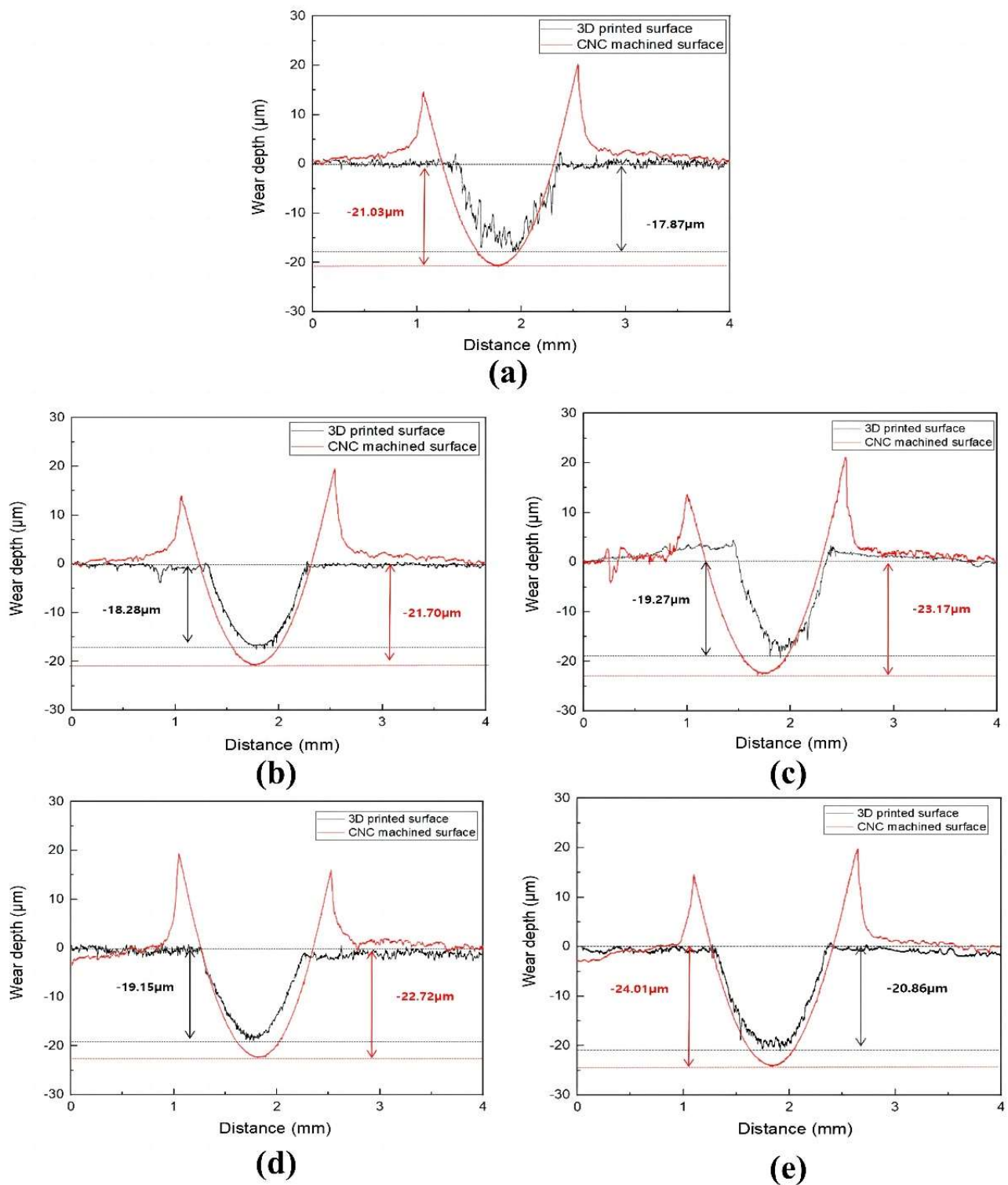


**Figure 11.** Wear scar profile plot of each control group. (a) Current = 0A; (b) Current = 0.8A, Al base; (c) Current = 0.8A, Steel base; (d) Current = 2.5A, Al base; (e) Current = 2.5A, Steel base.

**Table 5.** Summary of evaluation results for wear scar profiles.

Surface	Base	Current (A)	Wear Dept ( $\mu\text{m}$ )		Wear Width ( $\mu\text{m}$ )	
			Avg.	Sta. Dev	Avg.	Sta. Dev
Metal 3D printing	-	0	17.83	0.10	1292.84	8.43
Metal 3D printing	Aluminum alloy	0.8	18.32	0.13	1305.36	9.71
Metal 3D printing	Steel	0.8	19.18	0.18	1345.26	13.92
Metal 3D printing	Aluminum alloy	2.5	19.09	0.12	1328.19	12.31
Metal 3D printing	Steel	2.5	20.93	0.21	1390.26	14.84
CNC machining	-	0	21.06	0.08	1427.15	6.71
CNC machining	Aluminum alloy	0.8	21.76	0.09	1494.67	7.67
CNC machining	Steel	0.8	23.14	0.08	1614.64	8.98
CNC machining	Aluminum alloy	2.5	22.81	0.09	1556.49	9.04
CNC machining	Steel	2.5	24.13	0.14	1678.12	10.20

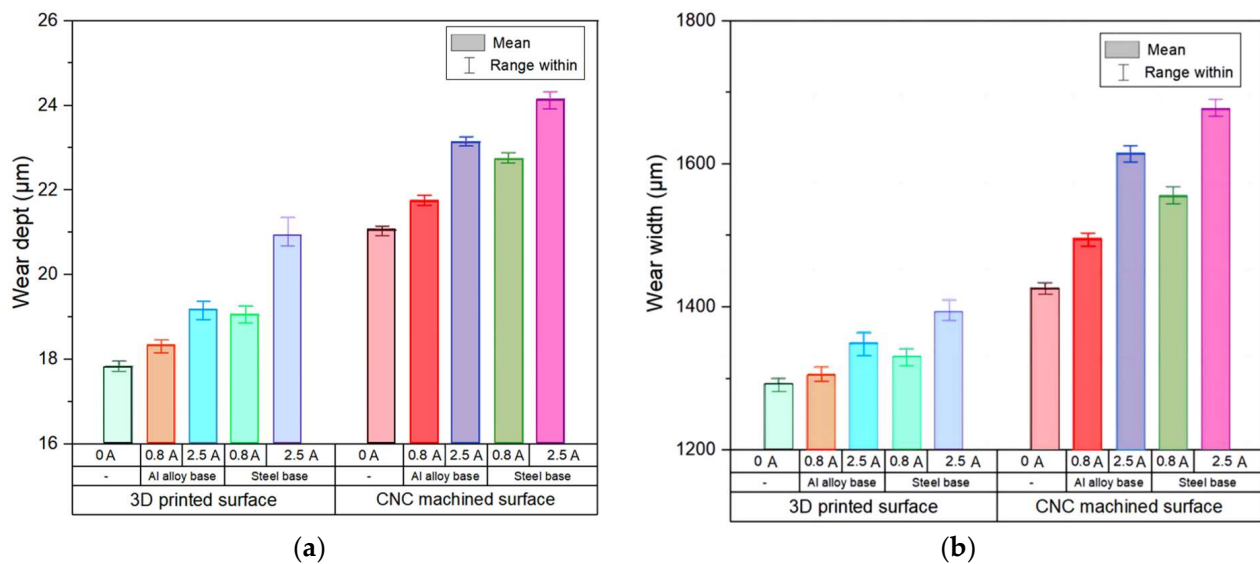
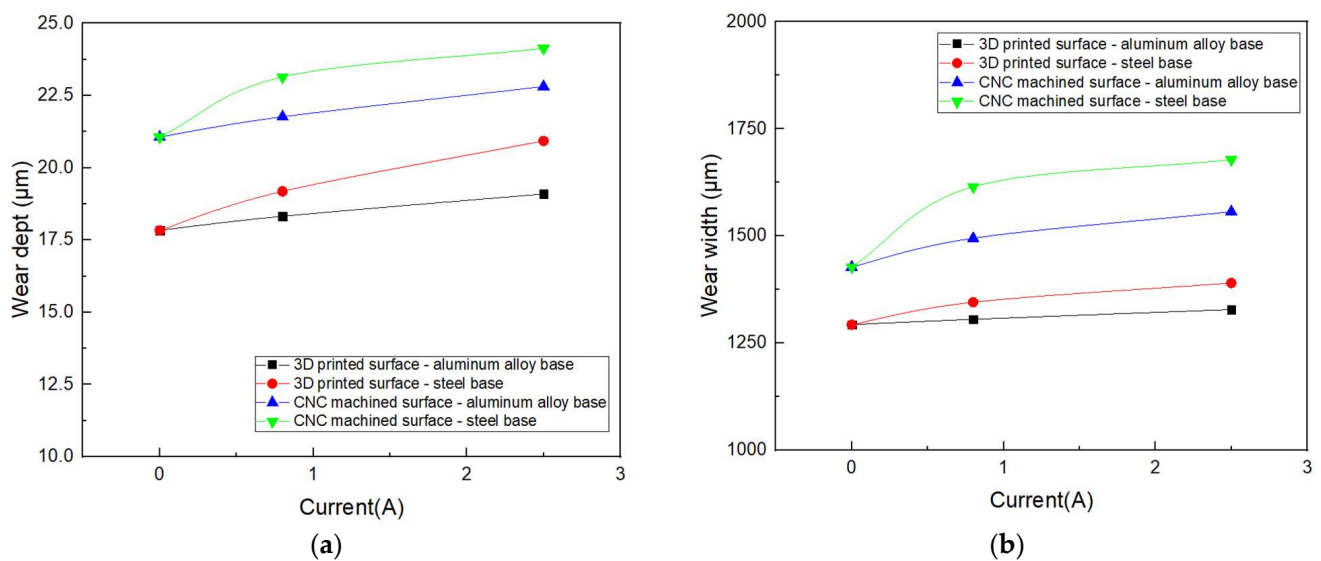
**Figure 12.** Histogram of wear data for different experimental groups. (a) Histogram of wear depth for different experimental groups, (b) histogram of wear width for different experimental groups.

Figure 13 illustrates the changes in wear width and depth of each combined sample under different currents. The increase in the friction coefficient between the ferromagnetic substrate and the metal 3D-printed surface sheet was greater than that of the CNC-machined surface sheet under the same current coil, and the wear marks on the metal 3D-printed surface were flatter and narrower than those on the CNC-machined surface. Therefore, metal 3D-printed surface sheets are more suitable as wear surfaces for magnetorheological devices. The evaluation results for 3D-printed surface panels had a greater error compared to CNC-machined surface panels, which may be attributed to greater variability in 3D-printed samples.





**Figure 13.** (a) Variation diagram of wear scar width; (b) variation diagram of wear scar depth.

The test point interval of 0.5 microns, calculate the product of the depth of each test point and the interval to determine the cross-sectional area of the wear area. Multiplying this sum by the friction test path gives the volume lost due to wear.

$$V_{loss} = 2\pi r \cdot d \sum n_1 + n_2 + \dots \quad (1)$$

The wear volume of the pure iron samples of each test group can be obtained through the above calculation formula. The calculated results were surprising. Although the wear depth and width of the CNC-machined surface after the wear test was much greater than that of the 3D-machined surface, the difference in wear volume between the two surfaces was small, as shown in Table 6 and Figure 14. The amount of surface wear of CNC machining was more stable.

**Table 6.** Wear volume calculation results for all experimental groups.

Surface	Base	Current(A)	Wear Volume (mm <sup>3</sup> )	
			Avg.	Sta. Dev
Metal 3D printing	-	0	1.7593	0.0172
Metal 3D printing	Aluminum alloy	0.8	1.8523	0.0184
Metal 3D printing	Steel	0.8	2.0694	0.0246
Metal 3D printing	Aluminum alloy	2.5	1.9746	0.0228
Metal 3D printing	Steel	2.5	2.6078	0.0348
CNC machining	-	0	1.7969	0.0054
CNC machining	Aluminum alloy	0.8	1.8699	0.0095
CNC machining	Steel	0.8	2.0376	0.0106
CNC machining	Aluminum alloy	2.5	1.9879	0.0086
CNC machining	Steel	2.5	2.4618	0.0118

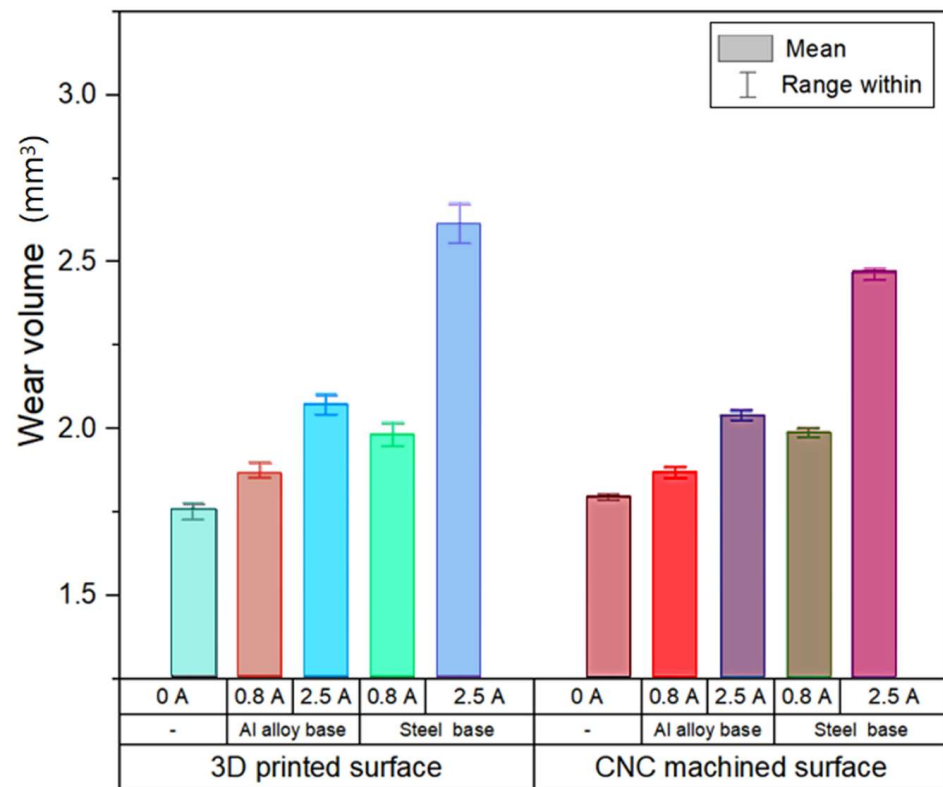


Figure 14. Histogram of wear volume for different experimental groups.

## 6. Conclusions

### 6.1. Ferromagnetic Base vs. Non-Ferromagnetic Base

The ANSYS magnetic flux analysis showed that the ferromagnetic base not only increased the magnetic field strength, but also changed its distribution in the energized coil, resulting in a concentrated magnetic field at the edge. This property was beneficial for improving the efficiency of magnetorheological devices, such as brake discs in magnetorheological brakes. The utilization rate of the magnetic field at the edge exceeded that at the center, highlighting the potential of ferromagnetic bases in improving the performance of electromagnetic coils. This finding had significant implications for research and applications in electromagnetic coil utilization. The maximum control improvement rate of the combined friction coefficient of the non-ferromagnetic base was 11.92%, while the maximum control improvement rate of the combined friction coefficient of the ferromagnetic base was 43.18%. According to the sensitivity of magnetorheological control of aluminum alloy base and steel base materials in magnetorheological fluid, different application ranges were adapted.

### 6.2. Metal 3D-Printed Surfaces vs. CNC-Machined Surfaces

Under identical conditions, the friction and wear test showed that the ferromagnetic base had higher combined friction coefficients and wear amounts compared to the non-ferromagnetic base. This discrepancy was due to variations in the distribution and magnitude of the magnetic field. The increase in friction coefficient was proportional to the increase in wear for both base combinations. However, the unique structure of the 3D-printed surface resulted in a lower initial coefficient of friction (no current) compared to the CNC-machined surface, indicating that the 3D-printed surface design reduces the frictional contact area and, consequently, the coefficient of friction. As the excitation current increased, the metal 3D-printed surface showed a superior improvement in the coefficient of friction compared to the CNC-machined surface. This was mainly due to the enhanced effect of magnetorheological adaptation resulting from the increased interaction of the

magnetorheological fluid (MRF) in the voids of the metal 3D-printed surface. The maximum control improvement rate of the combined friction coefficient of the CNC machining surface was 23.31%, and the maximum control improvement rate of the combined friction coefficient of the 3D-printed surface was 43.18%.

In addition, the wear test showed that under the same conditions, the depth and width of the wear marks on the metal 3D-printed surface were smaller than those on the CNC-machined surface. The CNC-machined surface was more prone to significant deformation. Although the calculated wear volume between the two surfaces showed minimal difference, the metal 3D-printed surface with its numerous voids showed less cumulative wear over time. This supports the feasibility of replacing CNC-machined surfaces with 3D-printed surfaces for magnetorheological devices and other applications using magnetorheological fluids. The maximum combined wear depth of the CNC-machined surface was 24.13  $\mu\text{m}$ , and the maximum width was 1678.12  $\mu\text{m}$ ; the maximum combined wear depth of the 3D-printed surface was 20.93  $\mu\text{m}$ , and the maximum width was 1390.26  $\mu\text{m}$ .

In conclusion, the optimal combination was to use a 3D-printed metal surface in conjunction with a ferromagnetic metal substrate. The increase rate of friction coefficient from 0.1459 at no current to 0.2089 at 2.5 A was 43.18%. This combination provided the most effective friction coefficient adjustment capability and comprehensive wear resistance. Its application provides an important benchmark for the optimization and advancement of magnetorheological devices.

**Author Contributions:** Conceptualization, D.L. and R.L.; methodology, R.L.; validation, formal analysis, investigation, resources, data curation and writing—original draft preparation, D.L.; writing—review and editing, D.L. and R.L.; supervision and project administration, C.-H.L. All authors have read and agreed to the published version of the manuscript.

**Funding:** This research was financially supported by the High-Level Foreign Expert Introduction Program (No. G2022035005L). This work was also supported under the framework of international co-operation program managed by the National Research Foundation of Korea (2022K2A9A2A06037454, FY2023).

**Data Availability Statement:** Since the data set was not created when the manuscript was submitted, the data cannot be viewed online for the time being.

**Conflicts of Interest:** All authors declare no conflict of interest in this article.

## References

1. Bozorth, R.M. *Ferromagnetism*; Wiley-IEEE Press: Hoboken, NJ, USA, 1993.
2. Jha, S.; Jain, V. Modeling and simulation of surface roughness in magnetorheological abrasive flow finishing (MRAFF) process. *Wear* **2006**, *261*, 856–866. [[CrossRef](#)]
3. Hajalilou, A.; Amri Mazlan, S.; Lavvafi, H.; Shamel, K. *Field Responsive Fluids as Smart Materials*; Springer: Singapore, 2016; p. 121.
4. Kumar, J.S.; Paul, P.S.; Raghunathan, G.; Alex, D.G. A review of challenges and solutions in the preparation and use of magnetorheological fluids. *Int. J. Mech. Mater. Eng.* **2019**, *14*, 13. [[CrossRef](#)]
5. Seo, Y.P.; Han, S.; Choi, J.; Takahara, A.; Choi, H.J.; Seo, Y. Searching for a Stable High-Performance Magnetorheological Suspension. *Mater. Res. Seoul Natl. Univ.* **2018**, *30*, 1704769. [[CrossRef](#)] [[PubMed](#)]
6. Li, Y.; Su, Z.; Luo, Y.; Wang, Y.; Luo, J.; Ji, D. Study on the friction and wear properties of magnetorheological fluids based on different lubricant formulas. *J. Supercond. Nov. Magn.* **2021**, *34*, 943–950. [[CrossRef](#)]
7. Thiagarajan, S.; Koh, A.S. Performance and stability of magnetorheological fluids—A detailed review of the state of the art. *Adv. Eng. Mater.* **2021**, *23*, 2001458. [[CrossRef](#)]
8. Zhang, P.; Lee, K.H.; Lee, C.H. Reciprocating friction characteristics of magneto-rheological fluid for aluminum under magnetic field. *Trans. Nonferrous Met. Soc. China* **2014**, *24*, 171–176. [[CrossRef](#)]
9. Quinci, F.; Litwin, W.; Wodtke, M.; van den Nieuwendijk, R. A comparative performance assessment of a hydrodynamic journal bearing lubricated with oil and magnetorheological fluid. *Tribol. Int.* **2021**, *162*, 107143. [[CrossRef](#)]
10. Góldasz, J.; Sapiński, B. *Insight into Magnetorheological Shock Absorbers*; Springer International Publishing: Cham, Switzerland, 2016; pp. 1–224.
11. Nakano, M.; Yang, J.; Sun, S.; Totsuka, A.; Fukukita, A. Development and Damping Properties of a Seismic Linear Motion Damper with MR Fluid Porous Composite Rotary Brake. *Smart Mater. Struct.* **2020**, *29*, 115043. [[CrossRef](#)]
12. Zhang, P.; Lee, K.H.; Lee, C.H. Wear Behavior of Rotary Lip Seal Operating in a Magnetorheological Fluid Under Magnetic Field Conditions. *J. Tribol.* **2018**, *140*, 22201. [[CrossRef](#)]

13. Zhang, P.; Lee, K.H.; Lee, C.H. Fretting friction and wear characteristics of magnetorheological fluid under different magnetic field strengths. *J. Magn. Magn. Mater.* **2017**, *421*, 13–18. [[CrossRef](#)]
14. Shahrivar, K.; Ortiz, A.; de Vicente, J. A comparative study of the tribological performance of ferrofluids and magnetorheological fluids within steel–steel point contacts. *Tribol. Int.* **2014**, *78*, 125–133. [[CrossRef](#)]
15. Vafadar, A.; Guzzomi, F.; Rassau, A.; Hayward, K. Advances in metal additive manufacturing: A review of common processes, industrial applications, and current challenges. *Appl. Sci.* **2021**, *11*, 1213. [[CrossRef](#)]
16. Cui, X.; Zhang, S.; Wang, C.; Zhang, C.H.; Chen, J.; Zhang, J.B. Microstructure and fatigue behavior of a laser additive manufactured 12CrNi2 low alloy steel. *Mater. Sci. Eng. A* **2020**, *772*, 138685. [[CrossRef](#)]
17. Bača, A.; Konečná, R.; Nicoletto, G.; Kunz, L. Influence of build direction on the fatigue behaviour of Ti6Al4V alloy produced by direct metal laser sintering. *Mater. Today Proc.* **2016**, *3*, 921–924. [[CrossRef](#)]
18. Buchanan, C.; Gardner, L. Metal 3D printing in construction: A review of methods, research, applications, opportunities and challenges. *Eng. Struct.* **2019**, *180*, 332–348. [[CrossRef](#)]
19. Wang, Y.; Wang, Y.T.; Li, R.D.; Niu, P.D.; Wang, M.B.; Yuan, T.C.; Li, K. Hall-Petch relationship in selective laser melting additively manufactured metals: Using grain or cell size? *J. Cent. South Univ.* **2021**, *28*, 1043–1057. [[CrossRef](#)]
20. Lam, L.P.; Zhang, D.Q.; Liu, Z.H.; Chua, C.K. Phase analysis and microstructure characterisation of AlSi10Mg parts produced by Selective Laser Melting. *Virtual Phys. Prototyp.* **2015**, *10*, 207–215. [[CrossRef](#)]
21. Zhang, H.; Wang, Y.; Wang, J.J.; Ni, D.R.; Wang, D.; Xiao, B.L.; Ma, Z.Y. Achieving superior mechanical properties of selective laser melted AlSi10Mg via direct aging treatment. *J. Mater. Sci. Technol.* **2022**, *108*, 226–235. [[CrossRef](#)]
22. Nasab, M.H.; Gastaldi, D.; Lecis, N.F.; Vedani, M. On morphological surface features of the parts printed by selective laser melting (SLM). *Addit. Manuf.* **2018**, *24*, 373–377. [[CrossRef](#)]
23. Liu, X.; Zhao, C.; Zhou, X.; Shen, Z.; Liu, W. Microstructure of selective laser melted AlSi10Mg alloy. *Mater. Des.* **2019**, *168*, 107677. [[CrossRef](#)]
24. Alghamdi, F.; Song, X.; Hadadzadeh, A.; Shalchi-Amirkhiz, B.; Mohammadi, M.; Haghshenas, M. Post heat treatment of additive manufactured AlSi10Mg: On silicon morphology, texture and small-scale properties. *Mater. Sci. Eng. A* **2020**, *783*, 139296. [[CrossRef](#)]
25. Oßwald, K.; Gissel, J.C.; Lochmahr, I. Macroanalysis of Hand Scraping. *J. Manuf. Mater. Process.* **2020**, *4*, 90. [[CrossRef](#)]
26. Liang, X.M.; Xing, Y.Z.; Li, L.T.; Yuan, W.K.; Wang, G.F. An experimental study on the relation between friction force and real contact area. *Sci. Rep.* **2021**, *11*, 20366. [[CrossRef](#)]
27. Kim, J.W.; Joo, B.S.; Jang, H. The effect of contact area on velocity weakening of the friction coefficient and friction instability: A case study on brake friction materials. *Tribol. Int.* **2019**, *135*, 38–45. [[CrossRef](#)]
28. Kumar, S.; Sehgal, R.; Wani, M.; Sharma, M.D. Stabilization and tribological properties of magnetorheological (MR) fluids: A review. *J. Magn. Magn. Mater.* **2021**, *538*, 168295. [[CrossRef](#)]
29. Li, H.; Jönkkäri, I.; Sarlin, E.; Chen, F. Temperature effects and temperature-dependent constitutive model of magnetorheological fluids. *Rheol. Acta* **2021**, *60*, 719–728. [[CrossRef](#)]
30. Ren, L.; Zeng, S.; Zhang, Y. Magnetic field characteristics analysis of a single assembled magnetic medium using ANSYS software. *Int. J. Min. Sci. Technol.* **2015**, *25*, 479–487. [[CrossRef](#)]

**Disclaimer/Publisher’s Note:** The statements, opinions and data contained in all publications are solely those of the individual author(s) and contributor(s) and not of MDPI and/or the editor(s). MDPI and/or the editor(s) disclaim responsibility for any injury to people or property resulting from any ideas, methods, instructions or products referred to in the content.